Selective-Synthesis of High-Performance Single-Crystalline $Sr_2Nb_2O_7$ Nanoribbon and $SrNb_2O_6$ Nanorod Photocatalysts

Di Chen and Jinhua Ye*

International Center for Materials Nanoarchitectonics, and Photocatalytic Materials Center, National Institute for Materials Science (NIMS), 1-2-1 Sengen, Tsukuba, Ibaraki 305-0047, Japan

Received December 23, 2008. Revised Manuscript Received April 1, 2009

Taking selective-synthesis of 1D single-crystalline $Sr_2Nb_2O_7$ nanoribbons and $SrNb_2O_6$ nanorods as an example, we demonstrated a general approach to synthesize niobium-contained nanostructured photocatalysts via a facile hydrothermal process. This method is based on reactions between soluble/insoluble metallic compounds and metallic oxide in the aqueous solution without using any organic dispersants or capping agents. The one-step technique is controllable and provides a simple, convenient, and innovative strategy for the preparation of niobate nanostructures and basically can be easily expanded to synthesize other materials with similar structure. Our results indicate that these as-synthesized 1D niobate nanostructures with larger BET surface areas possess higher photocatalytic activities for splitting pure water under UV light irradiation than those samples from the solid-state route.

Introduction

Photocatalytic splitting of water (H_2O) into H_2 and O_2 is an ideal way to produce H_2 and has been intensively studied as one of the possible ways to solve current energy and environmental issues during the past several decades.[1] To date, many kinds of photocatalysts based on the special electronic structure have been reported for water splitting under light irradiation, including oxides,[2−6] nitrides,[7−10] and sulfides.[10−13] However, development of a notable photocatalyst with high activity is urgently important to answer the demand for potential application in industrial fields. To improve the water-splitting abilities, one efficient way is to develop nanostructured photocatalysts[14−19] with extremely improved surface areas, because large surface area increases active sites at which the photocatalytic reaction occurs or small particle size decreases the distance that photogenerated electrons and holes migrate from bulk to reach active sites.

In this work, we present the selective synthesis of nanostructured photocatalysts $Sr_2Nb_2O_7$ nanoribbons and $SrNb_2O_6$ nanorods using a simple hydrothermal method. Both niobium-contained nanostructures show increased H_2 and O_2 evolution rates compared to those from the solid-state route, which further demonstrated that it is a feasible method to enhance the activities of catalysts by forming some catalysts with particular microstructures. Typically, we selected strontium niobate nanostructures as high performance water-splitting photocatalysts, mainly based on the following reasons. One is that many niobium-contained semiconductors have been proved to be effective photocatalysts due to the special structure construction in which [NbO_6] octahedral are distortable and the fairly high energy level of Nb 4d is beneficial for the potential hydrogen production by water splitting.[20−22] However, up to now, most of the niobate photocatalysts reported were synthesized from the solid-state reaction at high reaction temperature and long time, which basically had large size-distribution and small BET surface areas. The other is that 1D nanosized materials, which have rarely been fulfilled for niobate materials until now, are good systems for examining dimensionally confined and structurally well-defined physical and chemical phenomena and can provide useful platforms due to the relationship between their unique properties and particle size.

Experimental Section

Our method to selectively synthesize $Sr_2Nb_2O_7$ nanoribbons and $SrNb_2O_6$ nanorods is based on reactions between soluble/insoluble

* Corresponding author. Tel: +81 29 859 2646. Fax: +81 29 859 2301. E-mail: Jinhua.YE@nims.go.jp.

(1) Fujishima, A.; Honda, K. *Nature (London)* **1972**, *238*, 37.
(2) Zou, Z. G.; Ye, J. H.; Sayama, K.; Arakawa, H. *Nature (London)* **2001**, *414*, 625.
(3) Kanan, M. W.; Nocera, D. G. *Science* **2008**, *321*, 1072.
(4) Hata, H.; Kobayashi, Y.; Bojan, V.; Youngblood, W. J.; Mallouk, T. E. *Nano Lett.* **2008**, *8*, 794.
(5) Yao, W. F.; Ye, J. H. *Chem. Phys. Lett.* **2007**, *435*, 96.
(6) Graciani, J.; Nambu, A.; Evans, J.; Rodriguez, J. A.; Sanz, J. F. J. *Am. Chem. Soc.* **2008**, *130*, 12056.
(7) Lu, D. L.; takata, T.; Saito, N.; Inoue, Y.; Domen, K. *Nature (London)* **2006**, *440*, 295.
(8) Zhang, Q. H.; Gao, L. *Langmuir* **2004**, *20* (22), 9821.
(9) Haara, M.; Hitoki, G.; Takata, T.; Kondo, J. N.; Kobayashi, H.; Domen, K. *Catal. Today* **2003**, *78*, 555.
(10) Kato, H.; Kudo, A. *Angew. Chem., Int. Ed.* **2005**, *44*, 3565.
(11) Bang, J. H.; Richard, J. H.; Suslick, K. S. *Adv. Mater.* **2008**, *20*, 2599.
(12) Arai, T.; Senda, S.; Sato, Y.; Takahashi, H.; Shinoda, K.; Jeyadevan, B.; Tohji, K. *Chem. Mater.* **2008**, *20*, 1997.
(13) Chen, D.; Ye, J. H. *J. Phys. Chem. Solids* **2007**, *68*, 2317.
(14) Wang, G.; Lu, W.; Li, J. H.; Choi, J. Y.; Jeong, Y.; Choi, S.; Park, J.; Ryu, M. K.; Lee, K. *Small* **2006**, *2*, 1436.
(15) Chen, D.; Ye, J. H. *Adv. Funct. Mater.* **2008**, *18*, 1922.
(16) Chen, D.; Ye, J. H. *Chem. Mater.* **2007**, *19*, 4585.
(17) Fu, H. B.; Pan, C. S.; Yao, W. Q.; Zhu, Y. F. *J. Phys. Chem. B* **2005**, *109*, 22432.
(18) Song, S. Y.; Zhang, Y.; Xing, Y.; Wang, C.; Feng, J.; Shi, W. D.; Zheng, G. L.; Zhang, H. J. *Adv. Funct. Mater.* **2008**, *18*, 1.
(19) Hosogi, Y.; Kato, H.; Kudo, A. *Chem. Lett.* **2006**, *35*, 578.
(20) Kudo, A.; Kato, H.; Nakagawa, S. *J. Phys. Chem. B* **2000**, *104*, 571.
(21) Ebina, Y.; Tanaka, A.; Kondo, J. N.; Domen, K. *Chem. Mater.* **1996**, *8*, 2534.
(22) Zou, Z.; Ye, J.; Arakawa, H. *Chem. Phys. Lett.* **2001**, *333*, 57.

10.1021/cm8034714 CCC: $40.75
Published on Web 05/01/2009

Table 1. Selective Synthesis and Properties of 1D Niobates Nanostructures

sample[a]	Sr source/pH value	shape	S_{BET} (m^2/g)	E_g (eV)	rate (μmol/h·g) H_2	rate (μmol/h·g) O_2
$^{o}Sr_2Nb_2O_7$	$Sr(OH)_2$/13	ribbon	38	4.0	475	220
$^{m}SrNb_2O_6$	$Sr(AC)_2$/7.3	rod	9	3.9	435	205
$^{m}SrNb_2O_6$	$SrCO_3$/9.6	rod	8.5	3.9	–	–
$^{o}Sr_2Nb_2O_7$	$Sr(OH)_2 + (NH_4)_2CO_3$/13	platelet	–	–	–	–
$^{m}SrNb_2O_6$	$SrCO_3$/13	rod	–	–	–	–
$^{*}Sr_2Nb_2O_7$	SSR	particle	1.6	4.0	135	45
$^{*}SrNb_2O_6$	SSR	particle	0.2	3.8	70	20

[a] Superscripts: ^{o}, orthorhombic; ^{m}, monoclinic, *, synthesized from solid-state route.

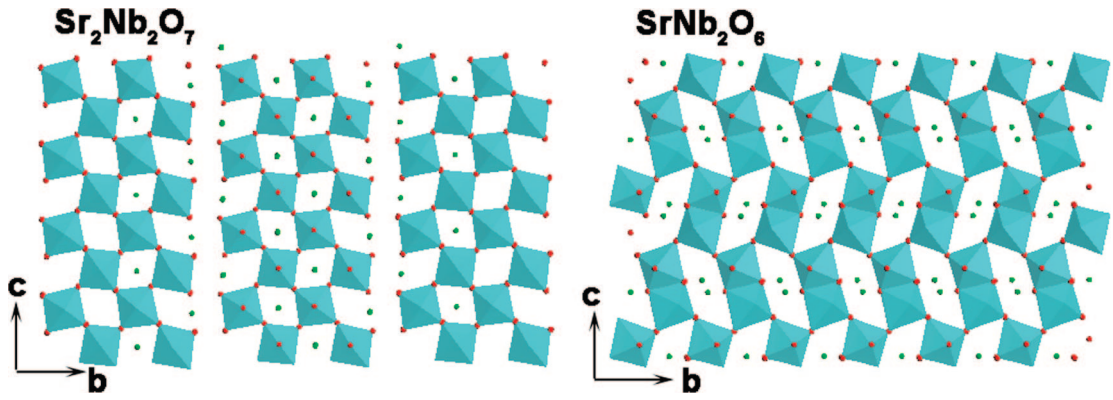

Figure 1. Crystal structures of $Sr_2Nb_2O_7$ and $SrNb_2O_6$ viewed along the *a*-axis. Small spheres and octagons represent Sr atoms and NbO_6 octahedra, respectively.

strontium compounds and niobium pentoxide in aqueous solution without using any organic dispersants or capping agents. In a typical procedure for $Sr_2Nb_2O_7$ nanoribbons, appropriate amounts of $Sr(OH)_2$ and Nb_2O_5 precursors with a mole ratio of 10:1 were added into 70 mL of distilled water under magnetic stirring. Then the mixtures were sealed in a Teflon-lined stainless steel autoclave and heated at 240 °C for 48 h. After cooling to room temperature, white product was washed with distilled water and 1 M HNO_3 for several times, respectively, and dried at 70 °C for 5 h. The synthesis process of $SrNb_2O_6$ nanorods was similar to that of $Sr_2Nb_2O_7$ nanoribbons except that $Sr(AC)_2$ was used as reagent (the mole ratio 1:1) and the reaction time was shorten to 24 h under the hydrothermal conditions (as shown in Table 1). Moreover, for comparison of photocatalytic activities, $Sr_2Nb_2O_7$ (at 1150 °C for 10 h) and $SrNb_2O_6$ (at 1400 °C for 24 h) were also prepared from the solid-state route, respectively (Table 1). The collected products were characterized by X-ray diffraction pattern (XRD; JEOL JDX-3500, Tokyo, Japan), SEM (JSM-6700F), HRTEM (JEM-3000F), UV−vis diffuse reflectance spectra (UV-2500, Shimadzu), and BET (Micromeritics, SHIMADZU). The photocatalytic reaction was performed in aqueous solution (catalyst, 0.2 g of RuO_2, 0.5 wt %; H_2O, 370 mL) with a closed gas circulation system. An inner irradiation type quartz cell with a 400 W high-pressure Hg lamp was employed. The evolved gas was determined by a thermal conductivity detector (TCD) gas chromatograph (Shimadzu GC-8A), which was connected to the system with a circulating line. The photonic efficiencies of H_2 evolution over $Sr_2Nb_2O_7$ and $SrNb_2O_6$ were measured by using an interference band-pass filter (λ_0 = 300.0 nm, T_{max} = 20.3%, $\Delta\lambda/2$ = 16.7 nm, Kenko). The light source was a 200 W Hg−Xe lamp, and a thermopile was used for measuring the intensity of incident light and then transferred to the number of incident photons. The apparent quantum yield (%) of H_2 was calculated by the equation QY (%) = $N_e/N_p = 2N_{H_2}/N_p$, where N_e is the number of reacted electrons, N_{H_2} is the number of H_2 molecules evolved, and N_p is the number of incident photons. In all experiments, the photocatalyst particles were suspended in solution by stirring with a magnetic stirrer, and the rotative velocity of the stirrer was set at 500 rpm.

Results and Discussion

Figure 1 shows the crystal structures of $Sr_2Nb_2O_7$ and $SrNb_2O_6$, respectively. Orthorhombic phase $Sr_2Nb_2O_7$ has a layered perovskite structure in which NbO_6 octahedra are connected by corner sharing, while monoclinic phase $SrNb_2O_6$ has a tunneled structure in which the octahedral NbO_6 are connected by sharing edges and corners. The as-prepared niobate nanostructures were first examined by powder XRD measurement, as illustrated in Figure 2. All of the diffraction peaks in the upper and lower patterns can be indexed to pure orthorhombic phase $Sr_2Nb_2O_7$ with space group $Cmc2_1$ (JCPDS 70-0114) and pure monoclinic phase $SrNb_2O_6$ with space group $P12_1/c$ (JCPDS 72-2088), respectively, which are good agreement with the standard patterns of samples (Figure S1, Supporting Information). The lattice parameters of products were also refined respectively as below: a = 3.928(8) Å, b = 26.893(1) Å, and c = 5.703(0) Å ($Sr_2Nb_2O_7$) as well as a = 7.031(2) Å, b = 5.348(6) Å, and c = 11.082(0) Å ($SrNb_2O_6$). They are a little larger than those of standards ($Sr_2Nb_2O_7$, a = 3.9330 Å, b = 26.7260 Å, c = 5.6830 Å; $SrNb_2O_6$, a = 7.722 Å, b = 5.592 Å, c = 10.9890 Å). No peaks of other impurities were observed, indicating satisfactory purity of the products. UV−vis diffuse reflectance spectra of the products were then recorded on a UV/vis spectrometer and were converted from reflection to absorbance by the standard Kubelka−Munk method. As depicted in Figure 3, the absorption edges of both nanostructures are steep due to band gap transitions from valence band to conduction band. The absorption peak positions in both spectra suggest that these materials are wide band gap

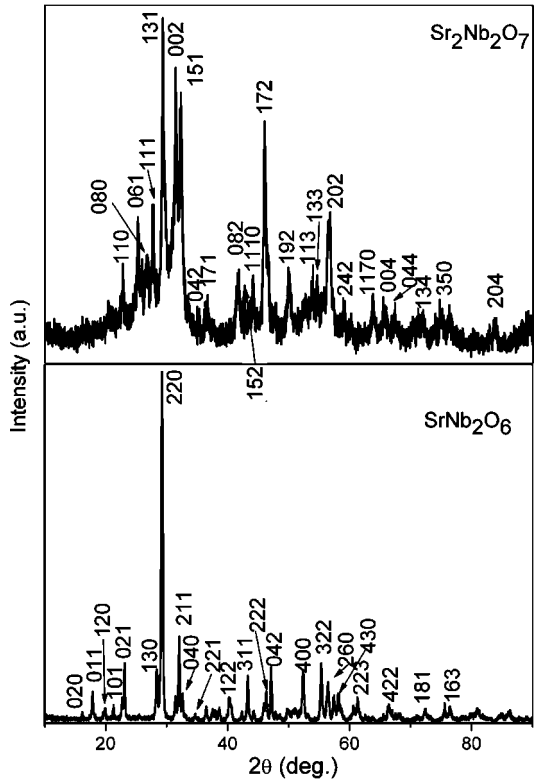

Figure 2. XRD patterns of $Sr_2Nb_2O_7$ and $SrNb_2O_6$ from the hydrothermal process.

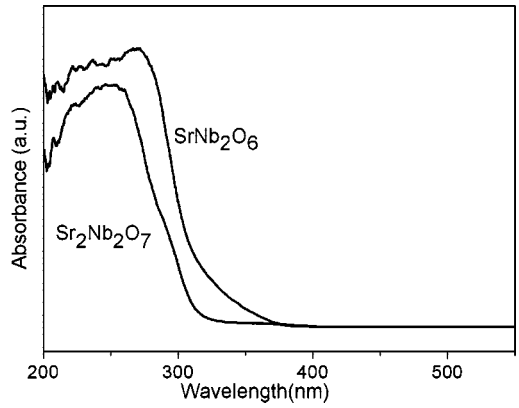

Figure 3. UV−visible spectra of as-synthesized $Sr_2Nb_2O_7$ and $SrNb_2O_6$ from the hydrothermal process.

semiconductors (as shown in Table 1). The band gaps can be estimated to be 4.0 eV for $Sr_2Nb_2O_7$ and 3.9 eV for $SrNb_2O_6$ from the onsets of the absorption, respectively, larger than the data of some reported literatures[23,24] (3.9 eV for $Sr_2Nb_2O_7$, and 3.6 eV for $SrNb_2O_6$). It is not surprising to observe the difference in the optical property because these two specimens have different constituting crystalline phases.

The morphology of as-synthesized $Sr_2Nb_2O_7$ product was examined by using field-emission scanning electron microscopy and transmission electron microscopy. We can easily see from Figure 4a that the produced $Sr_2Nb_2O_7$ are of smooth surface and with dominant 1D ribbonlike morphology, similar to many other reported 1D nanoribbons. The width of the nanoribbons is determined to range from 30 to 300 nm and the length could reach several tens of microns under the hydrothermal conditions. The thickness of the $Sr_2Nb_2O_7$ nanoribbons can be readily derived from some twisted ribbons, as shown in panels b and c of Figure 4, which is in the range of 20−30 nm. The TEM image of the $Sr_2Nb_2O_7$ product shown in Figure 4d also indicates their ribbonlike structure, similar to SEM results. The inset in Figure 4d is a typical selected-area electron diffraction (SAED) pattern recorded from a single ribbon; it can be indexed to be the $[1\bar{1}0]$ zone axis of orthorhombic $Sr_2Nb_2O_7$. These diffraction spots demonstrate the single crystallinity of this nanoribbon. The corresponding HRTEM image in Figure 4e shows that nanoribbons are structurally uniform with an interplanar spacing of about 0.52 nm, which corresponds to the (021) lattice spacing of $Sr_2Nb_2O_7$. Energy dispersive X-ray spectroscopy (EDX) attached to the TEM was employed for the qualitative elemental analysis of the $Sr_2Nb_2O_7$ nanoribbons, which shows the existence of Sr, Nb, and O elements.

Monoclinic $SrNb_2O_6$ nanorods can be successfully synthesized when using $Sr(AC)_2$ as starting material instead of $Sr(OH)_2$. Panels a and b of Figure 5 show typical SEM images of the produced $SrNb_2O_6$ sample. The products consisted of a large quantity of short nanorods with rectangular cross sections as the arrow indexed in Figure 5a. Typical nanorods have diameters of about 50−150 nm and the lengths are in the range of several microns. TEM images (Figure 5c and d) further confirm the rodlike shape of $SrNb_2O_6$ products, and distinctly rectangular ends can be clearly identified. The SAED pattern (inset) recorded from a single nanorod reveals the single-crystalline nature of the sample with the growth direction along the $[0\bar{1}1]$ zone axis. The corresponding HRTEM image (Figure 5e) shows two set of distinct fringe spacings of ca. 0.38 and 0.49 nm, respectively, which agree well with the separation between the (200) and (011) lattice planes of monoclinic $SrNb_2O_6$, respectively. These results indicate that the as-prepared $SrNb_2O_6$ nanorods are of good crystallinity with a growth direction parallel to the (100) plane. In our work, single crystalline $SrNb_2O_6$ nanorods with rectangle cross-section can also be prepared when using $SrCO_3$ as the source material. However, compared with the $SrNb_2O_6$ nanorods obtained from $Sr(AC)_2$, the nanorods obtained from $SrCO_3$ show large size distributions, as indicated in Figure 6a,b.

At room temperature, Nb_2O_5 is stable in the aqueous solution and no reactions take place. While under high-temperature hydrothermal condition, 240 °C in this case, Nb_2O_5 can easily ionize, dissolve, and react with other reagents to give $Sr_2Nb_2O_7$ nanoribbons and $SrNb_2O_6$ nanorods, respectively. Niobate nanostructures with different phases were selectively synthesized from different strontium precursors, indicating different reaction mechanisms, which can be described as follows.

In the $Sr(OH)_2-Nb_2O_5$ system, the following reaction takes place:

(23) Yoshino, M.; Kakihana, M. *Chem. Mater.* **2002**, *14*, 3369.
(24) Huang, T.; Lin, X. P.; Xing, J. C.; Wang, W. D.; Shan, Z. C.; Huang, F. Q. *Mater. Sci. Eng., B* **2007**, *141*, 49.

$$2Sr(OH)_2 + Nb_2O_5 \rightarrow 2H_2O + Sr_2Nb_2O_7 \text{ (nanoribbons)} \quad (1)$$

Under the high-temperature hydrothermal condition, both the choice of strong basic $Sr(OH)_2$ and the mole ratio of $Sr(OH)_2/Nb_2O_5$ are crucial factors to ensure the formation of 1D ribbonlike $Sr_2Nb_2O_7$ products. The starting material $Sr(OH)_2$ offers a strong basic condition (pH = 13, Table 1) and favors the nucleation of $Sr_2Nb_2O_7$, as proved by previous reports.[25] To investigate the influence of the mole ratio of $Sr(OH)_2$ and Nb_2O_5, we introduced $(NH_4)_2CO_3$ into the $Sr(OH)_2$ system to keep the pH value constant (pH = 13) and chose a lower $Sr(OH)_2/Nb_2O_5$ mole ratio of 5:1; the result shows that only $Sr_2Nb_2O_7$ products with plateletlike structure (see Supporting Information, Figure S2a) were prepared (XRD pattern shown in Figure S3, Supporting Information). A series of experiments was performed with a different initial $Sr(OH)_2/Nb_2O_5$ mole ratio at a fixed pH value (see Supporting Information Figure S4). The results can be summarized as follows. When the molar ratio was decreased to 5 or lower, for example, 2:1, no reaction happened and XRD analysis of the precipitate indicated that it was Nb_2O_5, instead of niobate. By adjusting the molar ratio to 5 and prolonging the reaction time to 3 days, plateletlike $Sr_2Nb_2O_7$ with poor crystallinity was prepared as described in the above discussions. When the $Sr(OH)_2/Nb_2O_5$ ratio was increased to 8:1, shorter nanoribbons with a few platelets were produced, as shown in the Supporting Information (Figure S4). Similar results have been reported by Yu et al. for the anisotropic growth of 1D $ZnWO_4$ products in a ligand-free hydrothermal crystallization process.[26] They proposed that, due to the unusual structural feature of crystal, the excess cations in solution resulted in both a greatly increased chemical potential and a fast growth rate along distinctive orientation. Therefore, we can conclude that the shape evolution of the nanoribbons that we observed here is similar to the formation of $ZnWO_4$ nanostructure, which is mainly governed by a general cooperative effect, including the intrinsic structural features of crystal and the foreign environment. Second, in the $Sr(AC)_2-Nb_2O_5$ system, the following reactions happen:

$$Sr(AC)_2 + 4O_2 \rightarrow SrCO_3 + 3H_2O + 3CO_2 \quad (2)$$

$$SrCO_3 + Nb_2O_5 \rightarrow CO_2 + SrNb_2O_6 \text{ (nanorod)} \quad (3)$$

If we directly used $SrCO_3$ instead of $Sr(AC)_2$, the reaction directly happens as follows:

$$SrCO_3 + Nb_2O_5 \rightarrow CO_2 + SrNb_2O_6 \text{ (nanorod)} \quad (4)$$

Since the autoclave was not completely filled with the precursor solution, the remaining space will be filled with

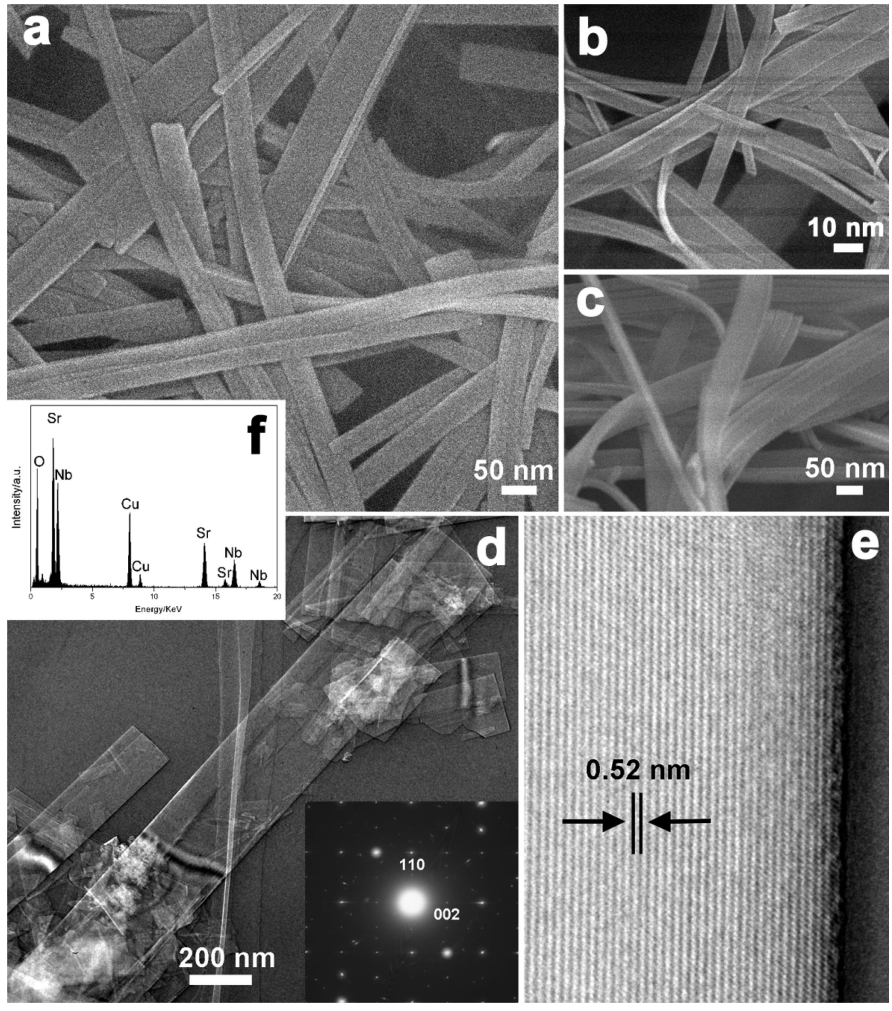

Figure 4. SEM and TEM images of as-synthesized $Sr_2Nb_2O_7$ nanoribbons in the $Sr(OH)_2$ system with the mole ratio of $Sr(OH)_2/Nb_2O_5$ = 10:1. (a−c) SEM images, (d) TEM images and SAED pattern (inset) of a single nanoribbon, (e) HRTEM image, and (f) EDS spectrum.

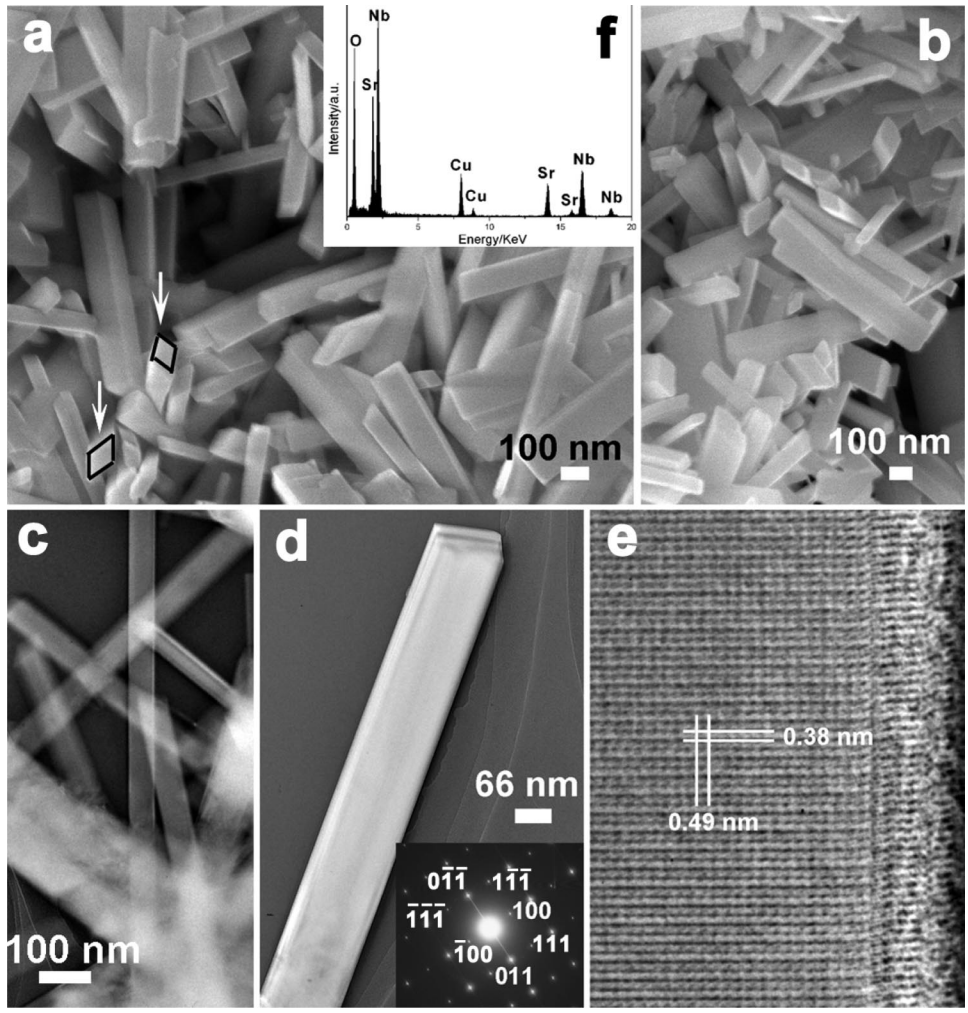

Figure 5. SEM and TEM images of as-synthesized $SrNb_2O_6$ nanorods from the $Sr(AC)_2$ system. (a, b) SEM images, (c, d) TEM images and SAED pattern (inset) of a single nanord, (e) HRTEM image, and (f) EDS spectrum.

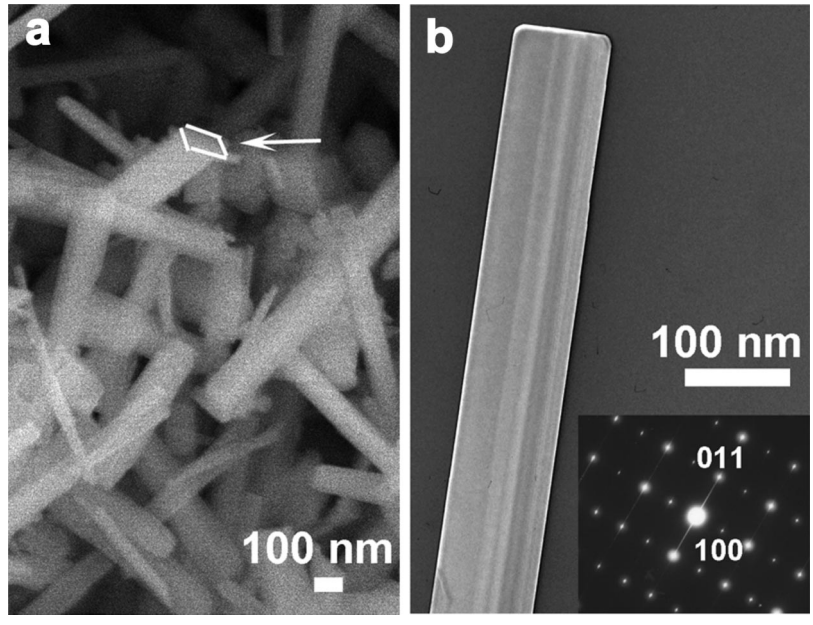

Figure 6. SEM and TEM images of as-synthesized $SrNb_2O_6$ nanorods from the $SrCO_3$ system. (a) SEM image and (b) TEM image and SAED pattern (inset) of a single nanorod.

compressed air. During the hydrothermal process, $Sr(AC)_2$ assisted by O_2 in the air in the solution slowly decomposed into $SrCO_3$, H_2O, and CO_2, and then the freshly formed $SrCO_3$ reacted with Nb_2O_5 immediately, resulting in $SrNb_2O_6$. Direct evidence for the formation of $SrCO_3$ is the XRD result of the product from $Sr(AC)_2$. It shows that it

was composed of $SrNb_2O_6$ and $SrCO_3$ compounds ($SrCO_3$ can be easily washed in acid solution), confirming the existence of $SrCO_3$. In $Sr(AC)_2$ or $SrCO_3$ system, the basicity of the solution was low and pH values were 7.3 and 9.6, respectively (Table 1), which is beneficial to the formation of $SrNb_2O_6$ products based on the discussion above.[25] We also adjusted the pH value of $SrCO_3$ system to 13, while pure $SrNb_2O_6$ products with rodlike structure were prepared and no other products were obtained. The Supporting Information shows the corresponding SEM image and XRD pattern (Figures S2b and S3, respectively). It is well-known that the K_{sp} of $SrCO_3$ (5.4×10^{-10}) is lower than that of $Sr(OH)_2$ ($K_{sp} = 6.4 \times 10^{-3}$), thus resulting in the lower concentration of Sr^{2+} active ions in the solution, which is obviously helpful to the nucleation and growth of Nb-rich $SrNb_2O_6$. This can also explain why no $SrNb_2O_6$ product was prepared in the $Sr(OH)_2 + (NH_4)_2CO_3$ system.

The surface areas of samples were measured on a Gemini 2360 surface area analyzer by nitrogen absorption at 77 K using the Brunauer−Emmett−Teller (BET) method. Relative to $Sr_2Nb_2O_7$ (1.6 m^2/g) and $SrNb_2O_6$ (0.2 m^2/g) synthesized by the solid-state route (Table 1), both $Sr_2Nb_2O_7$ nanoribbons and $SrNb_2O_6$ nanorods have larger surface areas of 38 m^2/g for $Sr_2Nb_2O_7$ nanoribbons and ~9 m^2/g for $SrNb_2O_6$ nanorods, respectively. It is speculated that nanostructured niobates with larger surface areas may possess higher activity than those samples from the solid-state route. Therefore, taking $Sr_2Nb_2O_7$ nanoribbons and $SrNb_2O_6$ nanorods as examples, we investigated the photocatalytic activities of catalysts for overall water splitting under UV light irradiation using an inner irradiation type Pyrex cell with a 400 W high-pressure Hg lamp. In this case, RuO_2 was loaded as cocatalyst on the surface of catalyst from the tetrahydrofuran (THF) $Ru_3(CO)_{12}$ solution by the impregnation method, followed by oxidation at 400 °C for 6 h. Figure S5 of the Supporting Information further shows typical TEM images of the surface structure of RuO_2-loaded $Sr_2Nb_2O_7$ catalysts. As black arrows indexed in panel a, RuO_2 spherical particles of a uniform size of about 15−20 nm dispersed fairly well on the catalyst surface. In the high-magnification image of panel b, a single RuO_2 island that is supposed to be an active site can be clearly seen on the surface of ribbonlike catalyst. Results of photocatalytic reaction also demonstrate that when RuO_2 was loaded onto niobates nanostructures, they exhibited notable activities for photocatalytically splitting of water into H_2 and O_2. The amounts of H_2 and O_2 produced over RuO_2−niobates are plotted as a function of time in Figure 7. The evolution rates of H_2 and O_2 were about 475 and 220 μmol/h·g for $Sr_2Nb_2O_7$ and 435 and 205 μmol/h·g for $SrNb_2O_6$, respectively, which were extremely higher than that for niobates from the solid-state route (Table 1.) Furthermore, corresponding ratios of H_2 and O_2 were 2.1 for $Sr_2Nb_2O_7$ nanoribbons and 1.9 for $SrNb_2O_6$ nanorods, respectively, close to the theoretical value of 2. The rates and ratios of produced H_2 and O_2 remained stable during two reaction runs, and the photonic efficiencies of the Pt-loaded $Sr_2Nb_2O_7$ nanoribbons and $SrNb_2O_6$ nanorods under 200 W Hg−Xe lamp irradiations amount to 32% and 19%, respectively. Furthermore, we also checked the photoactivity of RuO_2-loaded P25 for water splitting under the same experimental conditions. As shown in Figure S6 of the Supporting Information, only H_2 was generated with a weak evolution rate of about 85.5 μmol/h·g in the first run. In the second run, the rate of H_2 evolution decreased and no O_2 was still observed with the increase of time. These results proved that niobates had the ability to split water completely under light irradiation and had good stability in the photocatalytic reaction process.

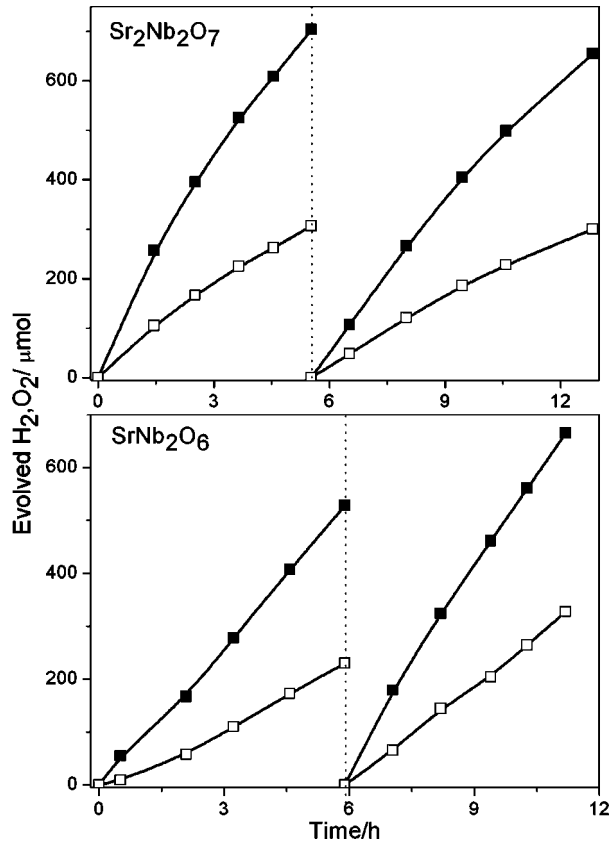

Figure 7. Photocatalytic pure water splitting over 0.5% RuO_2−niobate nanostructures under UV light irradiation (0.2 g of catalyst, 400-W Hg lamp, 370 mL of H_2O): ■, H_2; □, O_2.

Conclusion

In summary, 1D nanostructured niobate photocatalysts, $Sr_2Nb_2O_7$ nanoribbons and $SrNb_2O_6$ nanorods, have been selectively synthesized by a hydrothermal process by selecting different reaction systems. To obtain pure phase 1D niobate nanostructures with uniform dimensions, two key points should be mentioned. One is the choice of starting materials and the mole ratio of $Sr(OH)_2/Nb_2O_5$ for $Sr_2Nb_2O_7$ nanoribbons and the other is the solubility of source materials for $SrNb_2O_6$ nanorods, which control the growth kinetics for morphology evolution of as-synthesized nanostructures. Compared to niobates from the solid-state route, $Sr_2Nb_2O_7$ nanoribbons and $SrNb_2O_6$ nanorods with larger BET surface areas exhibit higher photocatalytic activity for overall water

(25) Lin, B.; Ma, J. F.; Yao, Y.; Liu, J.; Ren, Y.; Jiang, X. H.; Sun, Y.; Liu, Z. *J. Am. Ceram. Soc.* **2008**, *91*, 1329.
(26) Yu, S. H.; Liu, B.; Mo, M. S.; Huang, J. H.; Liu, X. M.; Qian, Y. T. *Adv. Funct. Mater.* **2003**, *13*, 639.

splitting under UV light irradiation. Principally, this hydrothermal process as a general method can be readily expanded to many niobium-containing photocatalysts with similar structure, and studies on the synthesis of other semiconductor materials are in progress.

Acknowledgment. This work was in part supported by World Premier International Research Center Initiative (WPI Initiative) on Materials Nanoarchitectonics, the Global Environment Research Fund, MEXT, Japan and the Strategic International Cooperative Program, Japan Science and Technology Agency (JST).

Supporting Information Available: Additional data for demonstrating growth mechanism of nanostructured products. This material is available free of charge via the Internet at http://pubs.acs.org.

CM8034714